Full paper

Strain engineering of the electrocatalytic activity of nitrogen-rich BeN$_4$ Dirac monolayer for hydrogen evolution reaction

Xiaoyong Yang [a], Rajeev Ahuja [a,b], Wei Luo [a,*]

[a] *Condensed Matter Theory Group, Materials Theory Division, Department of Physics and Astronomy, Uppsala University, Box 516, 75120 Uppsala, Sweden*
[b] *Department of Physics, Indian Institute of Technology Ropar, Rupnagar, Punjab, 140001, India*

A B S T R A C T

The strong bond energy and short bond length of N≡N triple bond make it a challenging target for synthesizing nitrogen-rich compounds. However, recent research has successfully fabricated atomic-thick BeN$_4$ layers under high pressure (Bykov et al., 2021). Beryllonitrene, a new 2D material, consists of a Be atom and polymeric nitrogen chains and has anisotropic Dirac cones located near the Fermi level. This distinguishes it from graphene, which has isotropic Dirac cones, bulk PtTe$_2$ and 2D borophene, which have Dirac cones located far from the Fermi energy. The anisotropic Dirac cones in beryllonitrene result in ultrahigh carrier mobility and the potential for direction-dependent quantum devices. In this study, we systematically investigated the hydrogen evolution reaction (HER) catalytic activity of nitrogen-rich, non-precious BeN$_4$ monolayer using first-principles DFT calculations. Our results demonstrate that BeN$_4$ monolayer is thermally stable, and Be vacancy is the most energetically favorable site for hydrogen adsorption. We also found the Gibbs free energy (ΔG_{H^*}) of H* coverage can be tuned to an optimal value of $|\Delta G_{H^*}| \leq 0.2$ eV through strain engineering, significantly enhancing the HER electrocatalytic activity of BeN$_4$ monolayer. Furthermore, we examined both the homolytic Tafel reaction and heterolytic Heyrovsky reaction for HER mechanism using reaction kinetics and AIMD simulations. These findings can contribute to the development of high-performance, non-precious, and nitrogen-rich 2D catalysts for HER in future research.

1. Introduction

The potential of nitrogen as a fuel or oxidizer in high-energy-density materials (HEDMs) has been extensively investigated due to its high heat of combustion and strong oxidizing ability [1]. However, the synthesis of nitrogen-rich compounds is a challenging task due to the inert nature of elemental nitrogen (N$_2$), its extremely strong triple bond, and the high reactivity of nitrogen-containing compounds. The N≡N triple bond has one of the highest bond energies among diatomic molecules, around 945 kJ/mol, and the bond length is relatively short, approximately 1.10 Å [2]. As a result, a significant amount of energy is required to overcome the strong attraction between the two nitrogen atoms, making it energetically unfavorable. Furthermore, nitrogen has low electronegativity and does not readily form stable chemical bonds with other elements, except for hydrogen, carbon, or oxygen, making it challenging to isolate and study the resulting products [3]. However, advances in high-pressure and high-temperature synthesis techniques are providing new opportunities for synthesizing and studying nitrogen-rich compounds [4–6].

Most recently, Bykov et al. reported the successful synthesis of bulk layered BeN$_4$ using the laser-heated diamond anvil cell technique under high-pressure, high-temperature conditions [6]. Specifically, the chemical composition BeN$_4$ was synthesized by laser heating of Be and N$_2$ at 85 GPa and ~2000 K, further transformed into BeN$_4$ layers after decompression to ambient conditions, interconnected via weak wan der Waals bonds [6]. The theoretical calculations reveal that the electronic lattice of BeN$_4$ monolayer is described by a slightly distorted honeycomb structure and its electronic structure exhibits anisotropic Dirac cones near the Fermi energy [6–8]. This is in stark contrast to other materials, such as graphene [9], where Dirac cones are isotropic, and bulk PtTe$_2$ crystal [10] and 2D borophene [11], where Dirac cones are located far from the Fermi energy. The presence of strongly anisotropic Dirac fermions at the Fermi energy in BeN$_4$ monolayer indicates the potential for realizing direction-dependent quantum devices and motivates an intense search for other material systems hosting anisotropic Dirac cones [6,12]. The Fermi velocities studied by Bykov et al. are 8×10^5 m/s along k_x direction and 3.06×10^5 m/s along k_y direction, respectively [6]. Additionally, BeN$_4$ monolayer has an anisotropic lattice thermal conductivity of 842.75 W m^{-1} K^{-1} in the armchair direction and 615.97 W m^{-1} K^{-1} along the

---

* Corresponding author.
E-mail address: wei.luo@physics.uu.se (W. Luo).

zigzag direction [8]. Moreover, BeN$_4$ monolayer exhibits an ultrahigh elastic modulus and mechanical strength, performing better than all other carbon-free 2D materials [7]. These remarkable properties make BeN$_4$ monolayer a promising candidate for materials research, inspiring researchers to explore its applicability as a catalyst for catalytic water splitting to enable efficient hydrogen production.

With the increasing demand for sustainable energy and the pressing environmental concerns, green hydrogen gas is considered to be the ultimate replacement for harmful fossil fuels, due to its elevated-energy density and zero carbon emissions during electrochemical combustion in air [13,14]. Besides, hydrogen also plays a central role in transforming CO$_2$ into useful hydrocarbon fuels, such as methanol [15]. The social demand on hydrogen is, therefore, expected to keep increasing in the future. Recently, technological advancements have been focused on developing viable methods for hydrogen production, with electrochemical water splitting being the simplest and most feasible way to achieve this goal [14,16]. The water-splitting mechanism involves two half-reactions: the hydrogen evolution reaction (HER), which is the reduction half-reaction ($2H^+ + 2e^- \rightarrow H_2$ (g)), and the oxygen evolution reaction (OER), which is the oxidation half-reaction ($2H_2O \rightarrow 4H^+ + 4e^- + O_2$). The theoretical potential required for this mechanism is 1.23 eV. However, due to substantial energy losses, commercial electrolyzers must operate at higher voltages than the ideal, resulting in overpotential [14,16,17]. Therefore, a good catalyst material is essential in reducing the overpotential of an electrochemical cell. Currently, catalytic water splitting for efficient hydrogen production accounts for only 4% of the world's hydrogen, with noble metals such as platinum (Pt) and its alloys, nickel (Ni) alloys, and other noble metals being promising catalysts for HER activity, which are the most expensive transition metals [18,19]. Therefore, the discovery of non-precious alternative catalysts towards HER with equivalent or better activities and stable durability has been a long-standing challenge [20,21].

All of the above-mentioned motivates us to study the catalytic properties of the BeN$_4$ monolayer by evaluating the hydrogen adsorption free energy, ΔG_{H^*}, which is a key intermediate of HER, using density functional theory (DFT) calculations. In detail, we carried out a structural optimization to determine the lattice parameters of BeN$_4$ monolayer, followed by a comprehensive exploration of its stability and electronic properties, including the electronic band structure and projected density of states. Of particular importance was our analysis of the adsorption of H at both the top of host atoms and vacancy sites. Our primary objective was to evaluate the catalytic potential of the BeN$_4$ monolayer and to elucidate the catalytic mechanism of the hydrogen evolution reaction (HER) by computing the Gibbs free energy of the H* intermediate. Furthermore, we employed a series of biaxial strains to modulate the catalytic performance of the BeN$_4$ monolayer. Our findings suggest that the BeN$_4$ monolayer has the potential to serve as an efficient electrocatalyst and that strain engineering represents an effective approach for further enhancing its catalytic performance.

2. Computational details

2.1. Total energy calculations

First-principles calculations based on density functional theory (DFT) [22] were performed using the *Vienna Ab initio Simulation Package* (VASP) [23,24]. The projector-augmented-wave (PAW) type pseudopotentials [25] were utilized to simulate the interaction of core electrons, while the Perdew–Burke–Ernzerhof (PBE) functional was employed to account for exchange–correlation energy within the Generalized Gradient Approximation (GGA) [26]. The effects of spin-polarization and van der Waals (vdW) interactions using the DFT-D3 method of Grimme [27] on the total energy of the 2D materials were considered in all the calculations. The Kohn-sham pseudo wavefunctions were expanded by plane waves with a cutoff energy of 550 eV. The ionic relaxation step was continued until the energy was converged

within 1×10^{-3} eV. The electronic convergence criterion for the ground state energy was set to 1×10^{-7}. A vacuum space of 25 Å was introduced to avoid interactions between images of the model system. The integration over the Brillouin zone (BZ) for unit cell and the $3 \times 3 \times 1$ supercell of the BeN$_4$ monolayer were carried out using a $21 \times 21 \times 1$ and a $7 \times 7 \times 1$ Monkhorst–Pack k-point mesh [28], respectively. To correctly describe the density of state (DOS), a $27 \times 27 \times 1$ Monkhorst–Pack k-point mesh was used. The dipole correction was included in all calculations of slab models. Furthermore, the work functions of the BeN$_4$ monolayer with and without hydrogen adatoms were determined using the equation, $\Delta\Phi = V_\infty - E_f$, where V_∞ is the electrostatic potential and E_f is the Fermi energy level [29].

2.2. Differential charge density and electron localization function

In this study, the calculation of charge density difference (CDD) involves the subtraction of the superimposed charge densities of ions or atoms from the total electron charge density of a crystal. However, due to the presence of different molecules absorbed on the layer BeN$_4$, the differential charge density was computed by subtracting the charge density of the layer from the superimposed charge densities of the two lattices, which were computed separately while maintaining a fixed the supercell geometry and the atomic positions. This approach enables the extraction of information regarding the interaction between the substrate and the molecule. Specifically, the charge density difference (CDD) is defined as follows,

$$\Delta\rho = \rho_{\text{Layer+Gas}} - \rho_{\text{Layer}} - \rho_{\text{Gas}}. \tag{1}$$

In addition to the aforementioned techniques, the electron localization function (ELF) [30,31] can also be utilized to evaluate electron localization in real space, and therefore, to provide insights into chemical bonding. ELF is defined as the ratio of the excess of kinetic energy density due to the Pauli exclusion principle, $t_p(r)$, and the Thomas–Fermi kinetic energy density $t_h(\rho) = \frac{1}{3}(3\pi)^{2/3}\rho^{5/3}$ of a homogeneous electron gas with density ρ. Thus, the increase in kinetic energy due to the Pauli principle can be determined by calculating,

$$t_p(r) = \frac{1}{2}\sum_i |\nabla\varphi_i|^2 - \frac{1}{8}\frac{|\nabla\rho(r)|^2}{\rho(r)}, \tag{2}$$

in which, the first term corresponds to the kinetic energy that is derived from the Kohn–Sham orbitals φ_i, while the second term represents the kinetic energy density associated with the same density distribution $\rho(r)$ in the absence of the Pauli exclusion principle.

Therefore, the ELF can be derived at any point r as the following expression,

$$\text{ELF} = \{1 + [\frac{t_p(r)}{t_h(\rho(r))}]^2\}^{-1}. \tag{3}$$

The electron localization function (ELF) is commonly presented as a contour plot that ranges between 0 and 1, with the upper limit indicating the highest degree of electron localization. Specifically, a low electron density region is observed near 0, while a homogeneous electron gas is represented by 0.5. Conversely, the region close to 1 is indicative of the presence of covalent electrons or lone-pair electrons. Moreover, to better understand the interaction between hydrogen and the BeN$_4$ monolayer, the Bader charge approach is employed to investigate the charge transfer [32].

2.3. AIMD simulations

To analyze the structural and energetic properties of the BeN$_4$ monolayer at finite temperature, we conducted *ab initio* molecular dynamics (AIMD) simulations in the canonical ensemble, employing constant volume and constant temperature (NVT) conditions [33]. The simulations were performed on $3 \times 3 \times 1$ supercell containing 45 atoms, and a temperature of 500 K was maintained using the Nosé

thermostat [34]. A time step of 1 fs was used for the AIMD calculations, which were carried out for 20000 ps to ensure adequate sampling of the thermal stability. Additionally, AIMD simulations were conducted at T = 300 K to verify the feasibility of hydrogen adsorption and desorption on the BeN$_4$ monolayer, based on the calculated hydrogen adsorption energies using DFT.

2.4. Gibbs free energy

Under conditions of standard state with pH = 0, $p(H_2)$ = 1 bar, and U = 0 V_{SHE}], the variation in Gibbs free energy for the adsorption of hydrogen (ΔG_{H^*}) can be computationally estimated as follows [29,35,36],

$$\Delta G_{H^*} = \Delta E_{H^*} - T\Delta S_{H^*} + \Delta E_{ZPE}, \tag{4}$$

where ΔE_{H^*} represents the adsorption energy that is gained upon the addition of a single hydrogen atom to the BeN$_4$ monolayer. ΔS_{H^*} and ΔE_{ZPE} correspond to the differences in entropy and zero-point energy (ZPE), respectively, between the adsorption of the hydrogen atom and hydrogen in the gas phase. Notably, ΔE_{H^*} can be computed using the following equation,

$$\Delta E_{H^*} = E_{Layer+nH^*} - E_{Layer+(n-1)H^*} - \frac{1}{2}E_{H_2}, \tag{5}$$

in which the variable n denotes the number of hydrogen atoms adsorbed on the BeN$_4$ monolayer. $E_{Layer+nH^*}$ and $E_{Layer+(n-1)H^*}$ represent the total energy of the BeN$_4$ monolayer with n and $n-1$ hydrogen atoms adsorbed, respectively. The asterisk (*) identifies the active site, which corresponds to the most stable adsorption position of hydrogen on the BeN$_4$ monolayer.

Additionally, the impact of vacancy effects of Be and N atoms on the catalyst efficiency was taken into account in this study. The formation energy of a vacancy defect is denoted as,

$$\Delta E_{def} = E_{V_i} - E_{Layer} + \Delta\mu_{V_i}, \tag{6}$$

in which E_{V_i} is the ground total energy of BeN$_4$ monolayer with a Be (or a N) vacancy defect, while E_{Layer} is the total energy of the defect-free BeN$_4$ monolayer. $\Delta\mu_{V_i}$ denotes the corresponding chemical potentials of Be and N elements in the hexagonal close-packed α phase with the axial ratio c/a = 1.571 and N_2 gas, respectively. The calculated formation energies of Be and N vacancies are 4.226 eV and 2.606 eV, respectively.

S_{H^*} is defined as,

$$T S_{H^*} = T S_{H^*} - \frac{1}{2} T S_o, \tag{7}$$

where $T S_{H^*}$ is the vibrational entropy of the hydrogen adatom on the BeN$_4$ monolayer, which has been previously established as 0.026 eV at 300 K. The S_o presents the vibrational entropy of the H$_2$ molecule, and the value of $T S_o$ is calculated as 0.41 eV. Consequently, $T\Delta S_{H^*}$ is estimated to be approximately −0.179 eV [37].

ΔE_{ZPE} is expressed as [38],

$$\Delta E_{ZPE} = E_{ZPT}^{nH} - E_{ZPT}^{(n-1)H} - \frac{1}{2}E_{ZPT}^{H_2}, \tag{8}$$

where E_{ZPT}^{nH} and $E_{ZPT}^{H_2}$ are the zero-point energy of n hydrogen atoms on the BeN$_4$ monolayer and single H$_2$ molecule in the gas phase. The vibration frequencies of hydrogen adsorption on the BeN$_4$ monolayer are determined to be 2724.128 cm^{-1}, 709.431 cm^{-1} and 673.096 cm^{-1}, while the calculated frequency of H$_2$ is 4334.0 cm^{-1}. Therefore, the Eq. (4) can be expressed as follows,

$$\Delta G_{H^*} = \Delta E_{H^*} + 0.419 \text{ eV}. \tag{9}$$

Based on the Sabatier principle, the ideal HER activity criterion is the proximity of the reaction Gibbs free energy for H* adsorption ΔG_{H^*} to zero [21,35,39]. Catalysts with a positive ΔG_{H^*} exhibit sluggish kinetics in the process of hydrogen adsorption, while a negative ΔG_{H^*} implies that the kinetics of H$_2$ release are relatively low [35,39–41].

2.5. The exchange current

Previously, the exchange current was analyzed based on Nørskov's assumption, which assumes that the rate-determining step of the hydrogen evolution reaction occurs via the Volmer step [35]. When the reaction Gibbs free energy for hydrogen adsorption (ΔG_{H^*}) is less than zero, the expression of exchange current (i_o) at pH = 0 can be written as follows,

$$i_o = -ek_o \frac{1}{1 + \exp(-\frac{\Delta G_{H^*}}{k_B T})}. \tag{10}$$

When $\Delta G_{H^*} < 0$, i_o at pH = 0 is evaluated as,

$$i_o = -ek_o \frac{1}{1 + \exp(\frac{\Delta G_{H^*}}{k_B T})}, \tag{11}$$

where k_o and k_B are the rate constant and the Boltzmann constant, respectively.

3. Results and discussion

3.1. Structural property and stability

The nitrogen-rich Dirac material, beryllonitrene (BeN$_4$) has been successfully synthesized using high-pressure synthesis techniques [6]. The rhombic primitive cell of the BeN$_4$ monolayer comprises one Be atom and four N atoms with the P2/m (No. 10) space group and point group of C2 h. Fig. 1(a) displays top and side views of the BeN$_4$ monolayer, along with its corresponding in-plane lattice vectors ($\vec{a}$ and $\vec{b}$), which are topographically flat. The BeN$_4$ monolayer consists of armchair-shaped polymeric N chains (N$_\infty$), which are bonded together by Be atoms from both sides, leading to an anisotropic network exclusively made of BeN$_4$ and Be$_2$N$_6$ [6,8,42]. At the same time, each N atom is triply connected to two N atoms and one Be atom, while Be exhibits a slightly distorted square-planar coordination. Specifically, the optimized lattice parameters are $|\vec{a}|$=3.661 Å, $|\vec{b}|$=4.271 Å, and γ=64.628 °, with two kinds of N-N bond lengths (l_{N-N}) of 1.343 Å and 1.338 Å, a Be-N bond length (l_{Be-N}) of 1.747 Å. All these parameter values are consistent very well with previous results [6–8,42,43].

Furthermore, the electron localization function (ELF) results, with an isovalue of 0.7 are depicted in Fig. 1(b) to study the electrostatic interaction of Be-N bonds in the BeN$_4$ monolayer. The ELF is a function that ranges from 0 to 1 at each point of the space. The results are in agreement with other DFT results [7,8], indicating that electrons are strongly localized on the N chains between neighboring N-N atoms and each N atom, pointing towards the Be atom. The ELF values between Be and N bonds are small, indicating a relatively strong ionic character. The electron cloud of anionic N$_\infty$ is strongly attracted to the Be metal, resulting in a relatively high covalent character of Be-N bonds. Additionally, Bader charge analysis was performed to examine the nature of the interaction between Be and N atoms in BeN$_4$ monolayer. Intriguingly, approximately 1.670 electrons are transferred from the Be atom to the N atom.

The electrostatic potentials of the BeN$_4$ monolayer under different strain-driven conditions along the Z-axis are shown in Fig. 2. Strain-driven variations to some extent affect the electrostatic potential of the BeN$_4$ monolayer, leading to a shift in the vacuum level. The charge redistribution induced by the strain-driven causes the electrostatic potential difference across the BeN$_4$ monolayer to decrease from 23.771 eV under 4% tensile strain to 26.824 eV under −4% compressive strain. Therefore, the surface state across the BeN$_4$ monolayer is altered by the strain-driven, which may extend the applications of monolayer BeN$_4$ in catalytic water.

The electronic properties of the BeN$_4$ monolayer are calculated using the PBE functional. The resulting band structure, total density of state (DOS) and projected density of states (PDOS) are shown in Fig. 1(c), which are found to be in good agreement with those reported
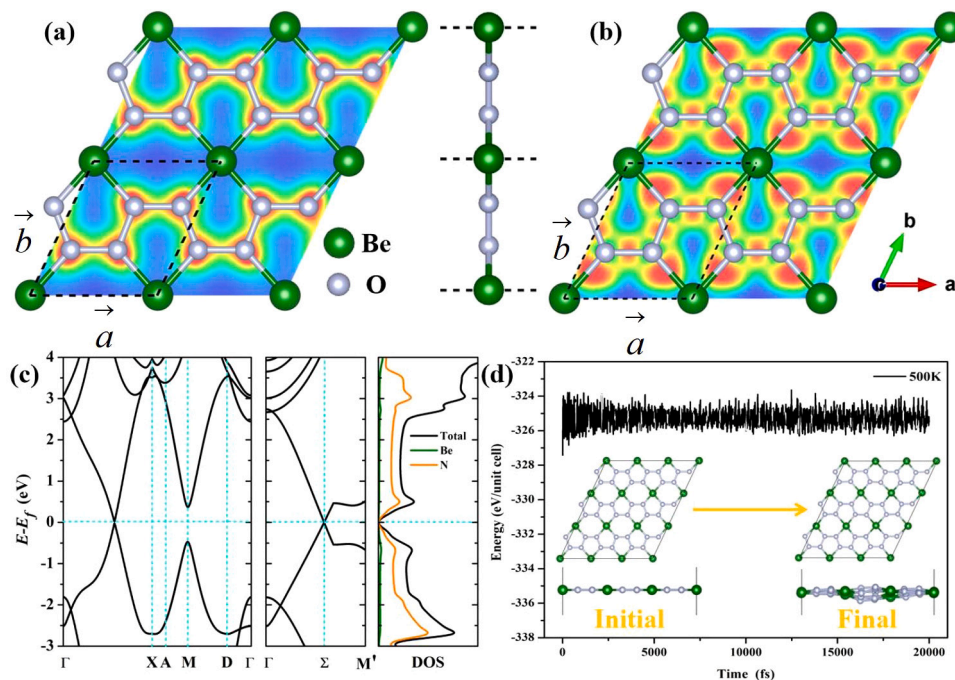
Fig. 1. (a) Top and side views of the optimized structure of BeN$_4$ monolayer. (b) Isosurfaces of the electron localization function (ELF) of BeN$_4$ monolayer with an isovalue of 0.7. (c) PBE band structure and total density of states (TDOS) as well as the corresponding projected density of states (PDOS). (d) The variation of the total energies of BeN$_4$ monolayer as a function of time under AIMD simulations at 500 K. Inner panel: top and side views of the snapshots are taken from the initial and final configurations of AIMD simulations at 500 K for BeN$_4$ monolayer, respectively.
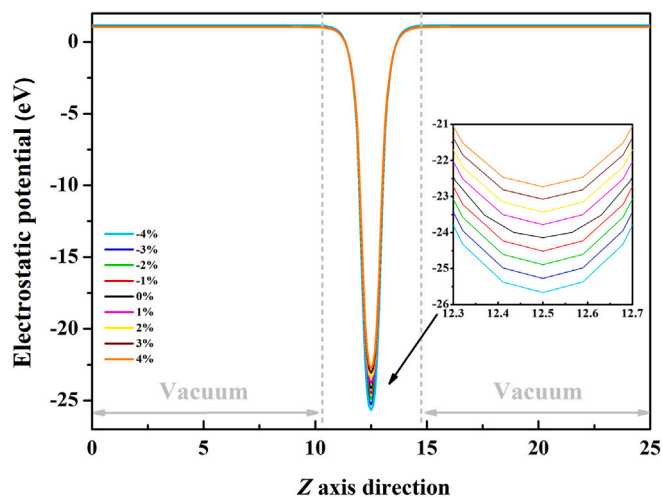

Fig. 2. Macroscopic electrostatic potential energies along the direction perpendicular to BeN$_4$ monolayer under different strains.

in previous studies [6–8,42,43]. The BeN$_4$ monolayer is observed to be a semimetal with a Dirac cone crossing at an off-symmetry k-point (Σ) located between the high symmetry points of Γ and X. It is widely recognized that Dirac cone band dispersion may lead to ultrahigh carrier mobility [7,44,45]. Mortazavi et al. [7] had previously predicted that the carrier mobility of the BeN$_4$ monolayer is 6.04×10^5 m/s (+25 eV/Å) along the κ_x direction and 2.92×10^5 m/s (± 12.06 eV/Å) along the κ_y direction. These findings suggest that the BeN$_4$ monolayer may be advantageous for separating charge carriers and achieving high performance in water splitting [46].

Analysis of the DOS and PDOS reveals that the band in the energy range of -2 eV to 3 eV is predominantly composed of the N (N-p_z) state with a small contribution from Be (Be-p_z) states. The positive slope band near the Fermi level is mostly contributed by N atoms to form a

π(N-N) state. In contrast, Be and N atoms almost equally contribute to the negative slope band, which displays hybridized states by $\pi*$(N-N) and π(Be-N) states.

Moreover, in order to investigate the thermal stability of the BeN$_4$ monolayer, *ab initio* molecular dynamics (AIMD) simulations were conducted at a temperature of 500 K for a period of 20000 fs. The outcomes of these simulations are presented in Fig. 1(d), which clearly indicate that the total energies of the system remained relatively constant around a fixed average value throughout the entire simulations. Notably, the inner panel of Fig. 1(d) reveals that the monolayer did not undergo any bond-breaking, but exhibited only slight structural distortion in the final configuration. Based on these findings, it can be inferred that the BeN$_4$ monolayer exhibits excellent thermal stability even at high temperatures.

3.2. HER activity

In order to study the catalytic performance of the BeN$_4$ monolayer, we have considered twenty-five possible adsorption sites of H* on a $3 \times 3 \times 1$ supercell with and without defects. These sites include the top sites of the Be and N atom, the top sites of B and N vacancies, the hexagonal center, and the bridge site between N and Be (or N) atoms, as depicted in Figure S1. The Gibbs free energies (ΔG_{H*}) of these sites for HER were calculated and the most favorable positions for HER are presented in Fig. 3(a). The most favorable position for HER in the defect-free BeN$_4$ monolayer is the top Be site with a ΔG_{H*} of 0.535 eV. The ΔG_{H*} values obtained for Be vacancy and N vacancy are -0.112 eV and 0.118 eV, respectively. The volcano top has a minimum value, implying the catalytic performance is optimal for HER. The volcano curve in Fig. 3(b) indicates intrinsic point defect significantly enhances the catalytic performance for the HER of the BeN$_4$ monolayer.

To investigate the charge transfer process following hydrogen adsorption on the BeN$_4$ monolayer, the Bader charge approach was utilized and the finding are presented in Fig. 4. The results demonstrate that the adsorption process leads to charge transfer between the hydrogen atom and the monolayer. Specifically, after adsorption on the
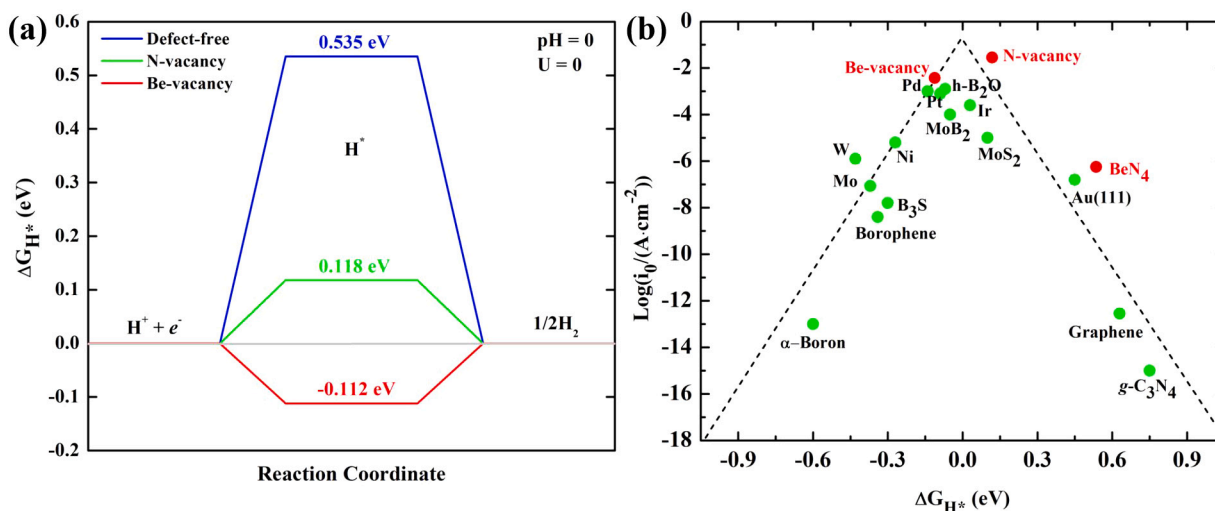
Fig. 3. (a) Adsorption free energy diagram for hydrogen evolution reaction on pristine and Be as well as *N* defective BeN$_4$ monolayer. (b) HER volcano curve including the BeN$_4$ monolayer and Be as well as *N* defective systems. The data for a variety of metals [47], MoS$_2$ [13], some boron materials [41,48–50], g-C$_3$N$_4$ [51] and graphene [52] are presented for comparison.
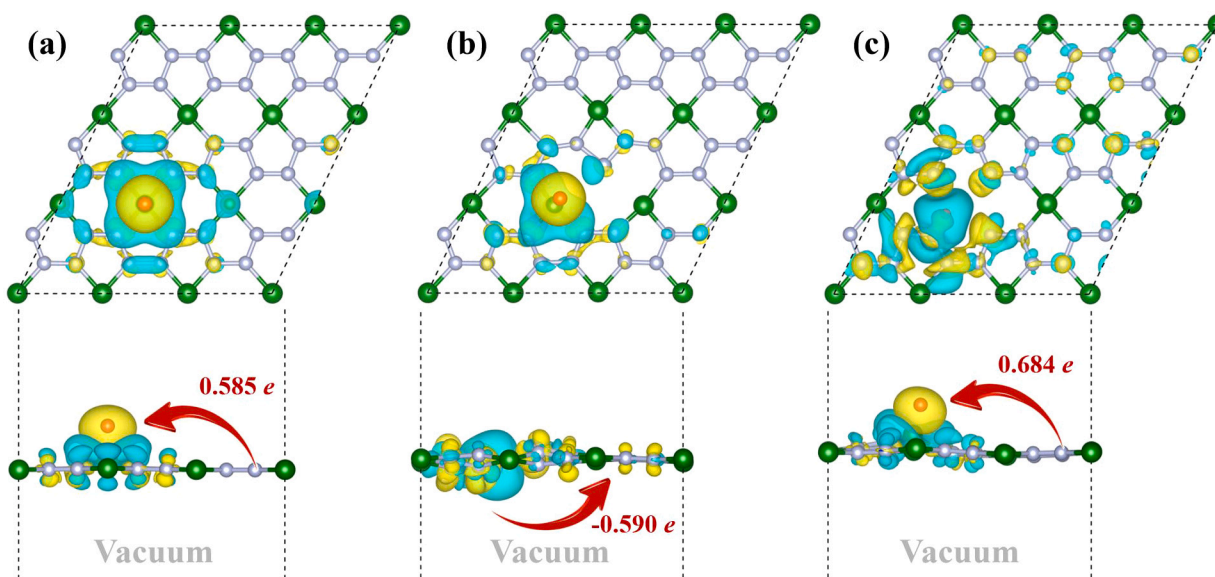

Fig. 4. Charge density difference (CDD) for the most advantageous position of a hydrogen atom on (a) defect-free BeN$_4$ monolayer, (b) Be vacancy monolayer, and (c) *N* vacancy monolayer, respectively. The yellow and cyan areas present charge accumulation and depletion, respectively. The red arrows show the orientation and the value of the charge transfer of hydrogen.

defect-free BeN$_4$ monolayer and N vacancy monolayer, the hydrogen gains 0.585 *e* and 0.684 *e*, respectively. This suggests that charge transfer occurs during the H$_2$ release process. In contrast, the hydrogen atom loses 0.590 *e* on the BeN$_4$ monolayer with a Be vacancy defect, indicating that the charge transfer occurs during the adsorption process. Notably, both defective and defect-free BeN$_4$ monolayers facilitate the transfer of a significant number of electrons to H*, ultimately approaching the chemical saturation charge of hydrogen (H$^+$). In the case of N vacancy, it is noteworthy that the ΔG_{H*} value decreases with an increasing charge transfer to H*, which is consistent with the charge transfer phenomenon observed on *h*-B$_2$O monolayer. It implies that the intensity of charge transfer plays a crucial role in the catalytic activity of HER [41]. Overall, the results demonstrate that defect engineering on BeN$_4$ monolayer is an effective approach for significantly enhancing the catalytic activity of HER compared to the defect-free monolayer.

Generally, the hydrogen evolution reaction (HER) process involves a two-electron transfer mechanism, that can follow the Volmer-Heyrovsky and Volmer–Tafel mechanisms [36,40]. Specifically, the initial step is

the adsorption of hydrogen, regardless of the mechanism being followed. This process is known as the Volmer reaction, wherein a proton receives an electron from the catalyst to form adsorbed hydrogen, and can be described as follows,

$$\text{Tafel}: \quad H^+ + e^- + * \rightarrow H^*. \tag{12}$$

In the context of catalysis, the asterisk symbol (∗) is often used to represent an active site on the surface of the catalyst material.

For the subsequent step, two possible reactions are known to occur, namely the homolytic Tafel reaction and the heterolytic Heyrovsky reaction. Under standard conditions of pH = 0 and *U* = 0, the homolytic Tafel reaction is expressed as [36,40],

$$H^* + H^* + e^- \rightarrow H_2. \tag{13}$$

The energy barrier for the reaction was calculated to be 0.351 eV, as illustrated in Fig. 5(a). Furthermore, the ground state energy of the final state is lower than that of the initial state, which can accelerate the
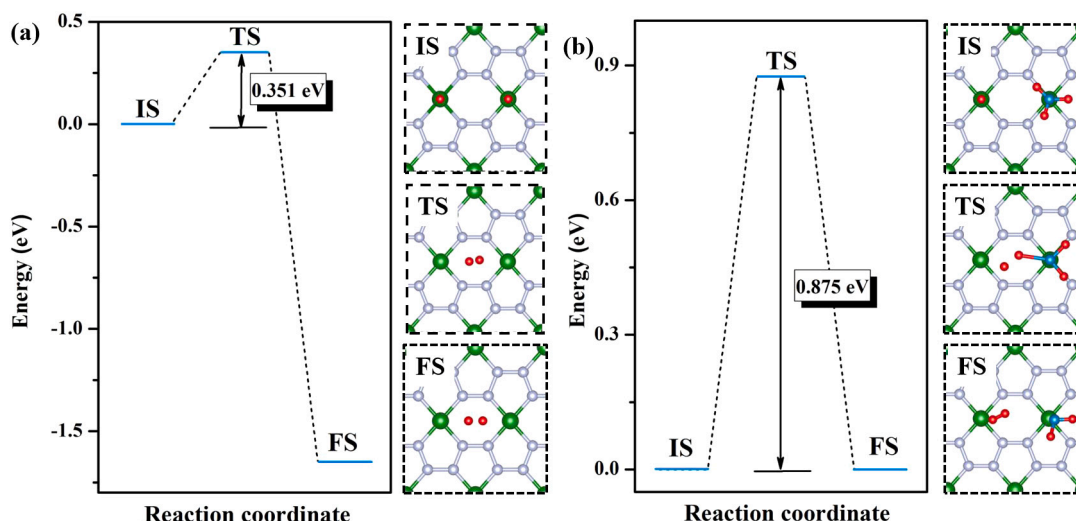
Fig. 5. Energy landscape of (a) homolytic Tafel reaction and (b) heterolytic Heyrovsky reaction on BeN$_4$ monolayer including the reaction configurations of the initial state (IS), transition state (TS), and final state (FS), respectively.

desorption of H$_2$. It is worth noting that the generated H$_2$ can swiftly move to the hexagonal centre of the BeN$_4$ monolayer, as depicted in the right panel of Fig. 5(a), indicating rapid H$_2$ release.

On the other hand, the heterolytic Heyrovsky reaction involves the generation of H$_2$ through the reaction of adsorbed H* with H$_3$O$^+$, as expressed [36,40],

$$H^* + H_3O^+ + e^- \rightarrow H_2 + H_2O. \qquad (14)$$

The calculated reaction energy barrier for the heterolytic Heyrovsky reaction is found to be 0.875 eV, as shown in Fig. 5(b), upon breaking away of a proton from the H$_3$O$^+$.

To validate the accuracy of the hydrogen adsorption energies obtained from DFT calculations and to investigate the feasibility of hydrogen adsorption and desorption, we performed *Ab initio* molecular dynamics (AIMD) simulations at $T = 300$ K on the BeN$_4$ monolayer. The AIMD simulations clearly demonstrate that hydrogen can spontaneously adsorb on the BeN$_4$ monolayer at 300 K, consistent with the DFT results (video clips in supplementary information). The specific AIMD simulations of hydrogen adsorption and desorption at 300 K, along with a schematic illustration of the BeN$_4$ monolayer are presented in Fig. 6

3.3. Effects of hydrogen coverage

Moreover, it is imperative to investigate the HER performance with respect to varying H* concentration. In this subsection, we have evaluated the Gibbs free energy (ΔG_{H^*}) by incrementally adding hydrogen atoms onto the defect-free BeN$_4$ surface. Specifically, for each added H atom, there are 18 equivalent binding sites (i.e., binding with Be atoms). Thus, we denote the H* coverage, θ, as $n/18$ (n=1-18), and have presented the most favorable configurations for different H* coverages in Fig. S2. The calculated Gibbs free energies (ΔG_{H^*}) for a range of adsorption configurations with H* coverage from 1/18 to 1 are presented in Fig. 7 after full relaxation. At H* coverages (θ) of 1/18, 1/6, 1/3, 1/2, 2/3, and 1, the calculated ΔG_H^* are 0.535, 0.647, 0.527, 0.547, 0.288 and 1.216 eV, respectively. These results suggest that the chemical adsorption of H* on the defect-free BeN$_4$ surface is challenging due to the weak binding of H* with the defect-free BeN$_4$ surface. Notably, Onlyat a coverage of 5/6, ΔG_{H^*} is significantly decreased to 0.075 eV, leading to the best HER catalytic performance. Furthermore, it is worth noticing that when an even number of H atoms are adsorbed on the defect-free BeN$_4$ surface, the entire system can be more stabilized by H* binding due to the higher symmetry. Consequently, ΔG_{H^*} at $\theta = 1/3$,

2/3 is slight lower than at $\theta = 1/18$, 1/6 and 1/2. Correspondingly, the HER activity affected by hydrogen coverage can be explained by the charge transfer based on the Bader charge analysis. As indicated in Table S1, fewer electrons are transferred to H* under $\theta > 1/18$ compared to $\theta = 1/18$, which suggests that a higher coverage could lead to relatively stronger Be-H bonding, and subsequently accelerate the H$_2$ adsorption on the defect-free BeN$_4$ surface. Nevertheless, it is worth mentioning that all ΔG_{H^*} under different θ are positive, indicating that the defect-free BeN$_4$ monolayer exhibits relatively slow kinetics in the process of hydrogen adsorption [35,39–41].

Furthermore, in order to comprehensively understand the variation of ΔG_{H^*} with the hydrogen coverage, we conducted an investigation on the total density of states (TDOS) as well as the projected density of states (PDOS) for the defect-free BeN$_4$ monolayer with the adsorbed hydrogen atoms. As depicted in Fig. 8, the TDOS peaks for all the hydrogen coverage models apparently cross the Fermi level. This result is primarily dominated by the N-p orbital, as demonstrated in Fig. S3. It is interesting to notice that the model with higher ΔG_{H^*} exhibits a relatively stronger intensity, such as $\theta = 1/18$, 1/6, and 1. On the contrary, the intensity peak of $\theta = 5/6$ configuration is the lowest, and the corresponding ΔG_{H^*} is the smallest with 0.075 eV. Besides, we notice that the Fermi level shifts from −2.747 eV to −4.677 eV with an increase in hydrogen coverage, which is consistent well with the results obtained for h-B$_2$O and B$_3$ monolayers affected by hydrogen coverage [41,48]. As evidenced by PDOS in Fig. S3, the activity of H-s mainly locates from −3 eV to −1 eV for $1 \le \theta \le 5/6$. Additionally, it can be observed that when the orbital hybridization between Be and H atoms is stronger in the range of −3 eV to −1 eV, the value of ΔG_{H^*} is also slightly smaller, such as $\theta = 2/3$ and 5/6, as shown in Fig. 7(a) and Fig. S3. This phenomenon is due to the transfer of electrons from the Be atom to these energy levels to hybridize with hydrogen atoms. The results adequately reveal the interaction between hydrogen and the BeN$_4$ monolayer. However, it is worth noting that the release of electrons from the BeN$_4$ monolayer is slow, as illustrated in Fig. 7(a). This observation is consistent with the interaction of Be and H atoms in the range of −3 eV to −1 eV, ultimately leading to the slow adsorption of hydrogen on the BeN$_4$ monolayer.

3.4. Tuning HER activity by strain-driven

Strain engineering has been demonstrated as an efficient approach to modifying the physical and chemical properties of two-dimensional (2D) materials, such as altering the redox band level [46,53]. Therefore, applying external strain may potentially affect the performance
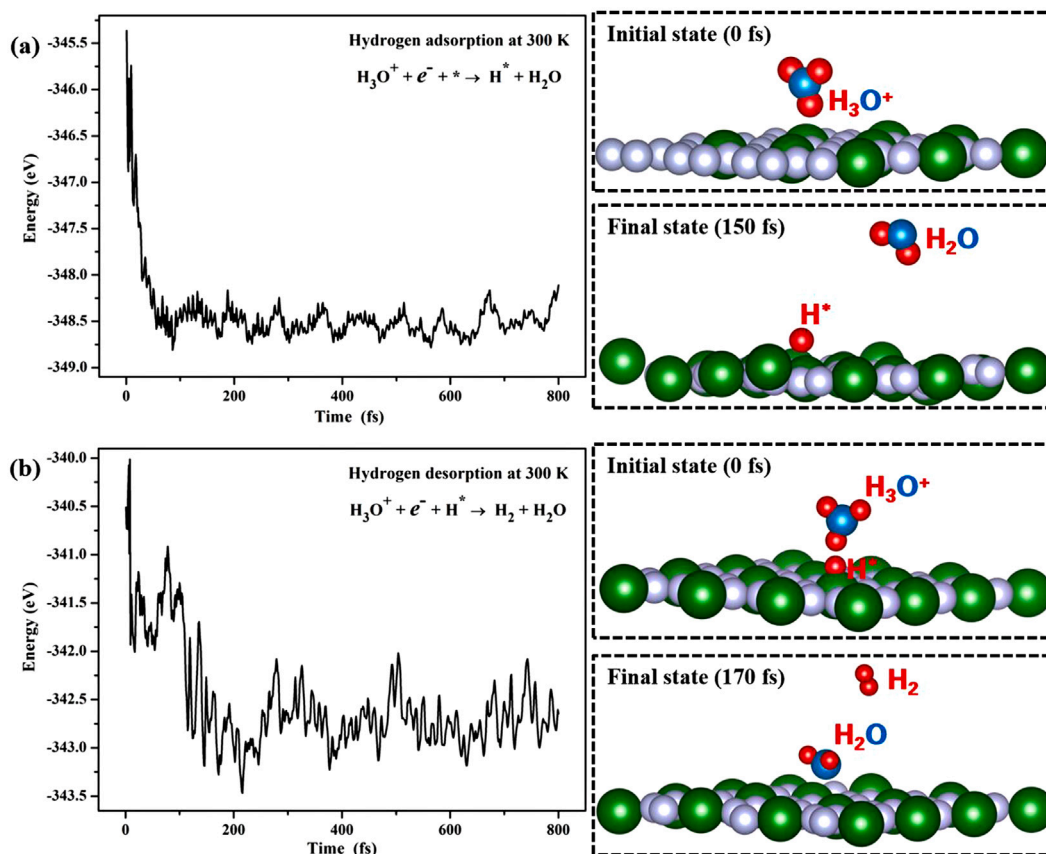
Fig. 6. Ab initio molecular dynamics simulation of (a) hydrogen adsorption and (b) desorption at 300 K on BeN$_4$ monolayer. AIMD simulations were carried out during 800 fs.
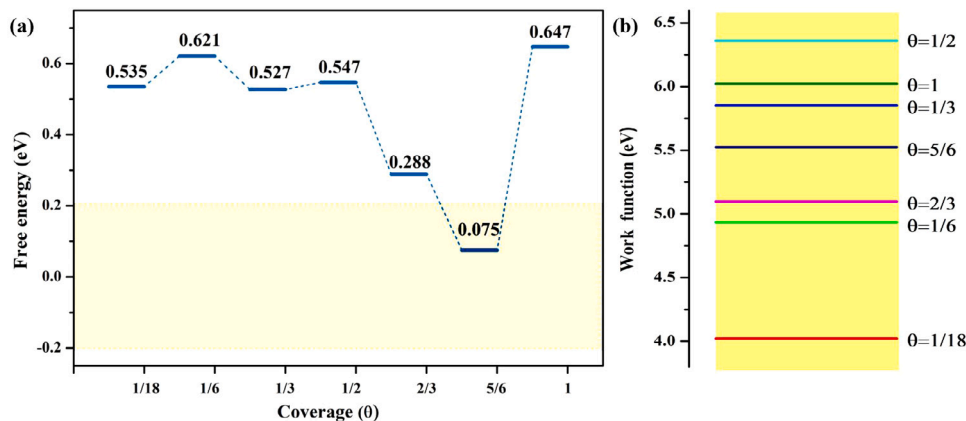

Fig. 7. (a) The free energy diagram of hydrogen evolution and (b) work functions on defect-free BeN$_4$ monolayer at different coverages of adsorbed hydrogens, respectively.

of the hydrogen evolution reaction. In this study, we systematically investigate the influence of small compressive/tensile strain (−4% to 4%) on the HER performance of the defect-free BeN$_4$ monolayer. The strain (δ) is defined as $\delta=(l_1 - l)/l$, where l_1 and l are the lattice parameters of the $3 \times 3 \times 1$ supercell with and without deformation, respectively. Specifically, compressive strain is defined as $-4\% \leq \delta <0$, and tensile strain is defined as $0< \delta \leq 4\%$. The variation of ΔG_{H*} with compressive/tensile strain on the BeN$_4$ monolayer is presented in Fig. 9, where the light yellow background area presents the HER activity of -0.2 eV $\leq \Delta G_{H*} \leq 0.2$ eV to judge whether a reaction site is HER active, as any undesirable thermodynamic condition within this specific set point can be reasonably compensated by a small applied potential in the electrochemical HER process or/and by a slight increase

in thermal energy through heating the electrochemical cell above room temperature [54,55].

Remarkably, both compressive and tensile strains can effectively enhance the HER performance for the system with weak H binding strength. It is observed that ΔG_{H*} decreases with the increase of compressive and tensile strain, as depicted in Fig. 9. Interestingly, $|\Delta G_{H*}|$ remains smaller than 0.2 eV over a relatively large strain range under $-2\% \leq \delta \leq 4\%$ at H* coverage of $\theta = 1/3$, $1/2$, and $5/6$, indicating high catalytic stability under realistic conditions. However, it is important to note that ΔG_{H*} exhibits an unusual tendency at H* coverage from $\theta = 1/18$ to 1 under the compressive strain of $\delta = -4\%$. It is attributed to the highly anisotropic mechanical response of BeN$_4$ monolayer compared to other MN$_4$ (M = Mg, Ir, Rh, and Pt) materials, as reported previously [7]. Under $\delta = -4\%$, the minimum ΔG_{H*} is -0.594 eV with
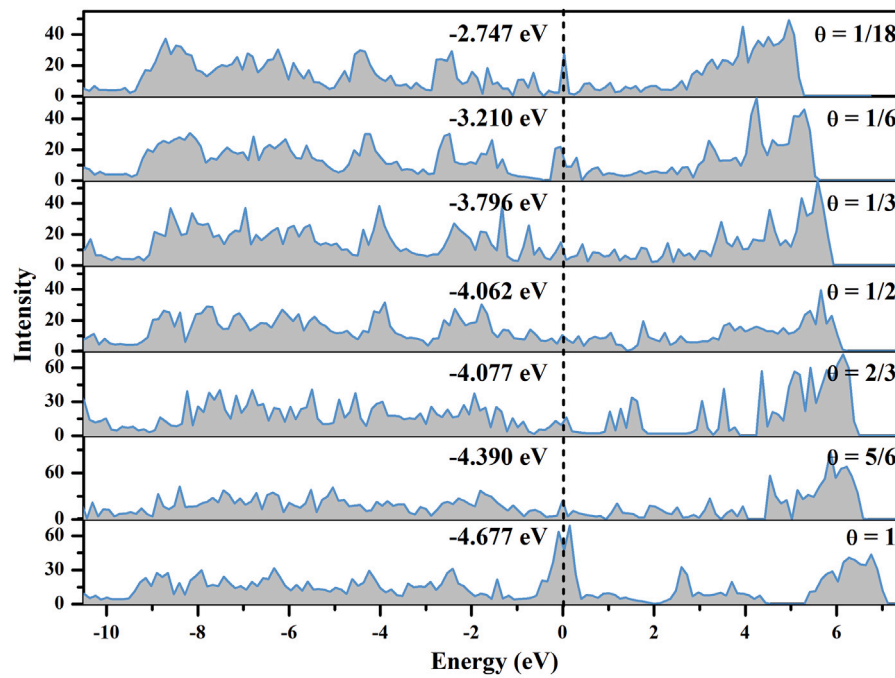
Fig. 8. Density of states of the defect free BeN$_4$ monolayer with adsorbed hydrogens. The black dashed line denotes the Fermi level position.
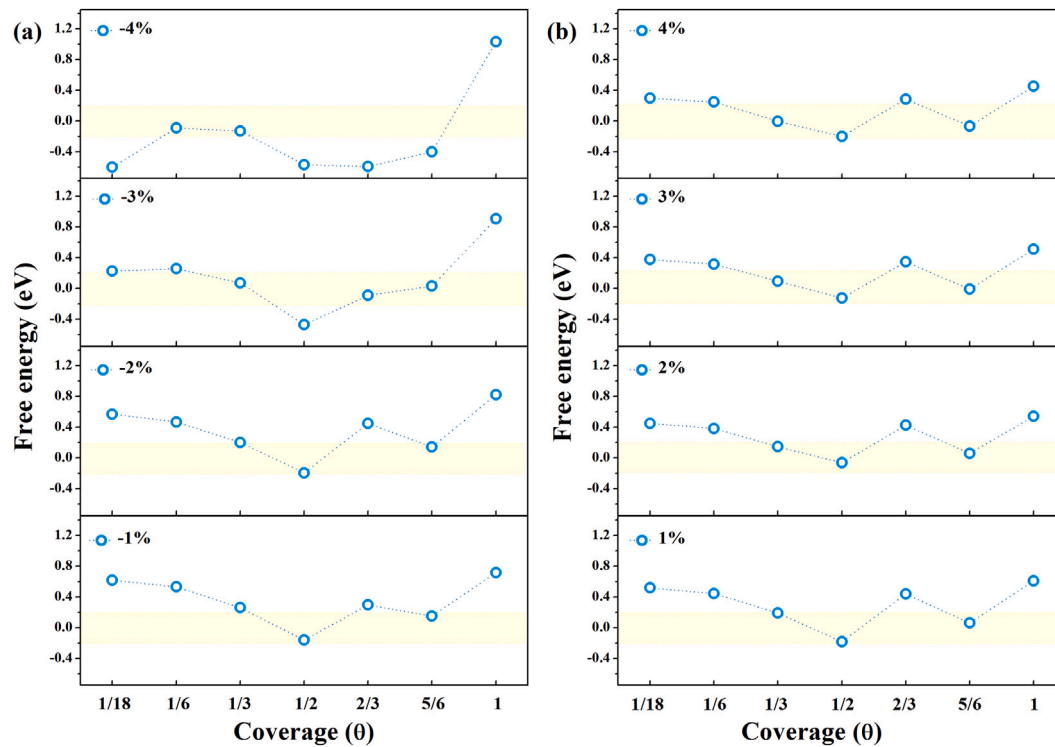

Fig. 9. Variation of the free energies of hydrogen adsorption with applied biaxial strain. The criteria as $|\varDelta G_{H^*}| \leq 0.2$ eV is set to judge the HER performance, which is highlighted in a light yellow area.

$\theta = 2/3$, indicating the poor HER activity due to strong hydrogen adsorption on the BeN$_4$ monolayer. Similarly, the maximum value of $\varDelta G_{H^*}$ is 1.032 eV under $\delta = -4\%$, indicating that hydrogen adsorption is blocked. The results indicate that only configurations of $\theta = 1/6$ and $1/3$ under $\delta = -4\%$ exhibit proximity to the thermoneutrality criterion based on $\varDelta G_{H^*}$. These findings suggest that the value of $\varDelta G_{H^*}$ for BeN$_4$

monolayer at different H* coverages can be manipulated to achieve a desired value by applying compressive or tensile strain.

To gain deeper insight into the effects of strain on the adsorption reaction, we calculated the density of state (DOS) of the BeN$_4$ monolayer with $\theta = 1/2$ and 1 adsorbed hydrogens. For low H* coverage $\theta = 1/2$, the Fermi level was observed to shift downwards with increasing
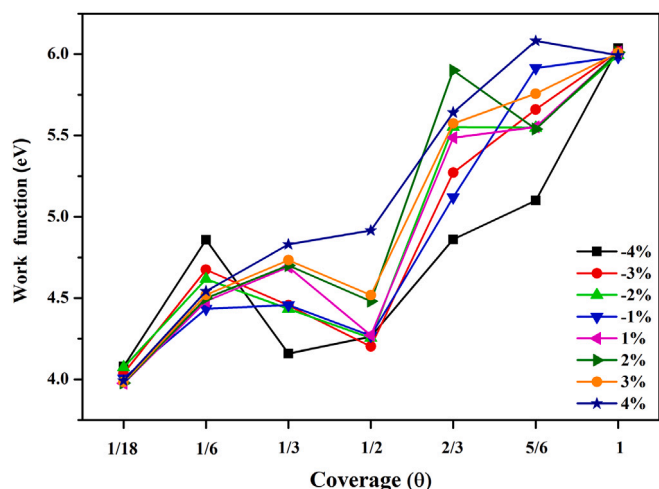
Fig. 10. Evolution of the work function of the defect free BeN$_4$ monolayer driven by hydrogen coverage under different strains.

compressive and tensile strain, as depicted in Fig. S4(a). Moreover, the hybridization between Be and H atoms slightly increased in the range of 0 eV and −3 eV, and the TDOS peaks crossed the fermi lever with minor contribution, which could potentially weaken the strength of N-H bond. On the contrary, for $\theta = 1$ case in Fig. S4(b), we observed a clear shift of electrons near the Fermi level towards the energy range of −4 eV to −2 eV, and larger electrons were also found to cross the Fermi level, thereby reducing the interaction between Be and H atoms and leading to higher ΔG_{H*}, as observed in Fig. 9.

To our knowledge, the work function of a material is highly susceptible to changes in surface morphology and the presence of impurities, which can greatly influence its HER activity [29]. Hence, in this study, we investigate the effect of strain on the variation of work function ($\Delta\Phi$) for different hydrogen-adsorbed BeN$_4$ configurations. Our results reveal a notable increase in $\Delta\Phi$ with increasing hydrogen coverage, especially for H* coverage from $\theta = 1/2$ to 2/3, as illustrated in Fig. 10. This suggests that the release rate of electrons from BeN$_4$ monolayer becomes more rapid. Notably, we observe that tensile strain induces a larger $\Delta\Phi$ than compressive strain for configurations with $\theta \geq 1/6$. For example, for $\theta = 1/2$ configuration, $\Delta\Phi$ is 4.263 eV under −4% strain-driven, whereas it sharply increases to 4.916 eV under 4% strain-driven. This trend is consistent with the Fermi level shift shown in Fig. S4, where the Fermi level shifts to a lower energy position under tensile strain compared to compressive strain.

4. Conclusion

Through the use of DFT calculations and AIMD simulations, the present study undertook a comprehensive investigation of the structural stability, electronic properties, and catalytic activities (active sites, adsorption, and reaction free energy diagram) of BeN$_4$ monolayer for the hydrogen evolution reaction (HER). The results confirm the thermal stability of BeN$_4$ monolayer. Besides, BeN$_4$ monolayer exhibit anisotropic Dirac cones in their electronic structure. Active sites on defective and defect-free configurations were thoroughly explored in order to evaluate their HER activity. The Gibbs free energy (ΔG_{H*}) was subsequently calculated using the active site with the lowest energy. Furthermore, the effects of hydrogen coverage and strain engineering on HER activity were studied. The volcano curves revealed that Be vacancy is the most favorable site for electrochemical reaction. The calculated ΔG_{H*} for the defect-free configuration was found to be 0.535 eV, indicating that the process of hydrogen adsorption requires energy. The reaction kinetics and AIMD simulations conducted at 300 K

suggest both homolytic Tafel reaction and heterolytic Heyrovsky reaction for HER mechanism can occur on BeN$_4$ monolayer. As increasing in H* coverage to $\theta = 5/6$, ΔG_{H*} is predicted as 0.075 eV, which has superior HER activity, indicating the HER activity is affected by hydrogen coverage. Moreover, ΔG_{H*} could be tuned to almost $|\Delta G_{H*}| \leq 0.2$ eV at coverage $\theta = 1/3$, 1/2, and 5/6 by both compressive and tensile strains. However, the hydrogen adsorption is hindered with $\theta = 1$ under strain-driven. Upon comparing the DOS of $\theta = 1/2$ and 1, it was found the high catalytic activity of $\theta = 1/2$ configuration under strain engineering is attributed to the strong orbital hybridization between Be and H atoms in the range of 0 to −3 eV. However, with an increase in hydrogen coverage to $\theta = 1$ under strain-driven, the corresponding orbital hybridization shifts to the lower energy area of −2 to −4 eV, leading to weaker interaction between Be and H atoms. This founding can offer valuable insights into the rational design of high-performance, non-precious, and nitrogen-rich 2D catalysts for HER.

CRediT authorship contribution statement

Xiaoyong Yang: Methodology, Validation, Investigation, Data curation, Writing – original draft, Funding acquisition. **Rajeev Ahuja:** Software, Resources, Writing – review & editing, Visualization, Funding acquisition. **Wei Luo:** Conceptualization, Methodology, Software, Investigation, Resources, Writing – review & editing, Visualization, Supervision, Project administration, Funding acquisition.

Declaration of competing interest

The authors declare that they have no known competing financial interests or personal relationships that could have appeared to influence the work reported in this paper.

Data availability

No data was used for the research described in the article.

Acknowledgments

Appendix A. Supplementary data

Supplementary material related to this article can be found online at https://doi.org/10.1016/j.nanoen.2023.108557. **Supporting Information Figure S1** The possible adsorption sites for a hydrogen atom on (a) pristine BeN$_4$ monolayer, (b) Be-defective monolayer, and (c) N-defective monolayer. **Figure S2** The table sites of hydrogen adsorbed on the defect-free BeN$_4$ monolayer with $3 \times 3 \times 1$ supercell. **Figure S3** Projected density of states (PDOS) of the defect-free BeN$_4$ monolayer with adsorbed hydrogens. The black dashed line denotes the Fermi level position. **Figure S4** The density of state of the defect-free BeN$_4$ monolayer with (a) $\theta = 1/2$ adsorbed hydrogens and (b) $\theta = 1$ adsorbed hydrogens under strain driven. The black dashed line denotes the Fermi level position. **Supplementary movie 1** Adsorption process. **Supplementary movie 2** Desorption process.

References

[1] A. Majumdar, X.Y. Yang, W. Luo, S. Chowdhury, S. Chakraborty, R. Ahuja, High exothermic dissociation in van der Waals like hexagonal two-dimensional nitrogen from first-principles molecular dynamics, Appl. Surf. Sci. 529 (2020) 146552.

[2] M.I. Eremets, A.G. Gavriliuk, I.A. Trojan, D.A. Dzivenko, R. Boehler, Single-bonded cubic form of nitrogen, Nature Mater. 3 (2004) 558–563.

[3] C. Mailhiot, L.H. Yang, A.K. Mcmahan, Polymeric nitrogen, Phys. Rev. B 46 (1992) 14419–14435.

[4] M. Bykov, K.R. Tasca, I.G. Batyrev, D. Smith, K. Glazyrin, S. Chariton, M. Mahmood, A.F. Goncharov, Dinitrogen as a universal electron acceptor in solid-state chemistry: An example of uncommon metallic compounds $Na_3(N_2)_4$ and NaN_2, Inorg. Chem. 59 (2020) 14819–14826.

[5] M. Bykov, E. Bykova, A.V. Ponomareva, I.A. Abrikosov, S. Chariton, V.B. Prakapenka, M.F. Mahmood, L. Dubrovinsky, A.F. Goncharov, Stabilization of polynitrogen anions in tantalum nitrogen compounds at high pressure, Angew. Chem. Int. Edn 60 (2021) 9003–9008.

[6] M. Bykov, T. Fedotenko, S. Chariton, D. Laniel, K. Glazyrin, M. Hanfland, J.S. Smith, V.B. Prakapenka, M.F. Mahmood, A.F. Goncharov, A.V. Ponomareva, F. Tasni, A.I. Abrikosov, T.B. Masood, I. Hotz, A.N. Rudenko, M.I. Katsnelson, N. Dubrovinskaia, L. Dubrovinsky, I.A. Abrikosov, High-pressure synthesis of Dirac materials: layered van der Waals bonded BeN_4 polymorph, Phys. Rev. Lett. 126 (2021) 175501.

[7] B. Mortazavi, F. Shojaei, X. Zhuang, Ultrahigh stiffness and anisotropic Dirac cones in BeN_4 and MgN_4 monolayers: a first-principles study, Mater. Today Nano 15 (2021) 100125.

[8] M. Wang, D. Han, Thermal properties of 2D Dirac materials MN_4 (M=Be and Mg): A First-Principles Study, ACS Omega 7 (2022) 10812–10819.

[9] K.S. Novoselov, A.K. Geim, S.V. Morozov, D. Jiang, Y. Zhang, S.V. Dubonos, I.V. Grigorieva, A.A. Firsov, Electric field effect in atomically thin carbon films, Science 306 (2004) 666–669.

[10] M. Yan, H. Huang, K. Zhang, E. Wang, W. Yao, K. Deng, G. Wan, H. Zhang, M. Arita, H. Yang, Z. Sun, H. Yao, Y. Wu, S. Fan, W. Duan, S. Zhou, Lorentz-violating type-II Dirac fermions in transition metal dichalcogenide $PtTe2$, Nature Commun. 8 (2017) 257.

[11] B. Feng, O. Sugino, R.Y. Liu, J. Zhang, R. Yukawa, M. Kawamura, T. Iimori, H. Kim, Y. Hasegawa, H. Li, L. Chen, K. Wu, H. Kumigashira, F. Komori, T.C. Chiang, S. Meng, I. Matsuda, Dirac fermions in borophene, Phys. Rev. Lett. 118 (2017) 096401.

[12] J. Kim, S.S. Baik, S.H. Ryu, Y. Sohn, S. Park, B.G. Park, J. Denlinger, Y. Yi, H.J. Choi, K.S. Kim, Observation of tunable band gap and anisotropic Dirac semimetal state in black phosphorus, Science 349 (2015) 723–726.

[13] S.H. Noh, J. Hwang, J. Kang, M.H. Seo, D. Choi, B. Han, Tuning the catalytic activity of heterogeneous two-dimensional transition metal dichalcogenides for hydrogen evolution, J. Mater. Chem. A 6 (2018) 20005–20014.

[14] D. Saraf, S. Chakraborty, A. Kshirsagar, R. Ahuja, In pursuit of bifunctional catalytic activity in PdS_2 pseudo-monolayer through reaction coordinate mapping, Nano Energy 49 (2018) 283–289.

[15] Z. Weng, J. Jiang, Y. Wu, Z. Wu, X. Guo, K.L. Materna, W. Liu, V.S. Batista, G.W. Brudvig, H. Wang, Electrochemical CO_2 reduction to hydrocarbons on a heterogeneous molecular Cu catalyst in aqueous solution, J. Am. Chem. Soc. 138 (2016) 8076–8079.

[16] K. Zeng, D. Zhang, Recent progress in alkaline water electrolysis for hydrogen production and applications, Prog. Energy Combust. Sci. 36 (2010) 307–326.

[17] J. Rossmeisl, A. Logadottir, J.K. Nørskov, Electrolysis of water on (oxidized) metal surfaces, Chem. Phys. 319 (2005) 178–184.

[18] J. Greeley, T.F. Jaramillo, J. Bonde, I.B. Chorkendorff, J.K. Nørskov, Computational high-throughput screening of electrocatalytic materials for hydrogen evolution, Nature Mater. 5 (2006) 909.

[19] J.H. Shim, Y.S. Kim, M. Kang, C. Lee, Y. Lee, Electrocatalytic activity of nanoporous Pd and Pt: effect of structural features, Phys. Chem. Chem. Phys. 14 (2012) 3974.

[20] X.Y. Yang, A. Banerjee, Z.T. Xu, Z.W. Wang, R. Ahuja, Interfacial aspect of $ZnTe/In_2Te_3$ heterostructures as an efficient catalyst for the hydrogen evolution reaction, J. Mater. Chem. A 7 (2019) 27441.

[21] X.Y. Yang, D. Singh, R. Ahuja, Recent advancements and future prospects in ultrathin 2D semiconductor-based photocatalysts for water splitting, Catalysts 10 (2020) 1111.

[22] W. Kohn, L.J. Sham, Self-consistent equations including exchange and correlation effects, Phys. Rev. 140 (1965) A1133.

[23] B. Hammer, L.B. Hansen, J.K. Nørskov, Improved adsorption energetics within density-functional theory using revised Perdew–Burke–Ernzerhof functionals, Phys. Rev. B 9 (1999) 7413.

[24] G. Kresse, J. Furthmüller, Efficient iterative schemes for *ab initio* total-energy calculations using a plane-wave basis set, Phys. Rev. B 54 (1996) 11169.

[25] P.E. Blöchl, Projector augmented-wave method, Phys. Rev. B 50 (1994) 17953.

[26] J.P. Perdew, K. Burke, M. Ernzerhof, Generalized gradient approximation made simple, Phys. Rev. B 77 (1996) 3865.

[27] S. Grimme, Semiempirical GGA-type density functional constructed with a long-range dispersion correction, J. Comput. Chem. 27 (2006) 1787–1799.

[28] H.J. Monkhorst, J.D. Pack, Special points for Brillouin-zone integrations, Phys. Rev. B 13 (1976) 5188.

[29] X.Y. Yang, A. Banerjee, R. Ahuja, Structural insight of the frailty of 2D Janus NbSeTe as an active photocatalyst, ChemCatChem 12 (2020) 6013–6023.

[30] A.D. Becke, K.E. Edgecombe, A simple measure of electron localization in atomic and molecular systems, J. Chem. Phys. 92 (1990) 5397–5403.

[31] A. Savin, O. Jepsen, J. Flad, O.K. Andersen, H. Preuss, H.G. von Schnering, Electron localization in solid-state structures of the elements: the diamond structure, Angew. Chem. Int. Edn 31 (1992) 187–188.

[32] E. Sanville, S.D. Kenny, R. Smith, G. Henkelman, Improved grid-based algorithm for bader charge allocation, J. Comput. Chem. 28 (2007) 899–908.

[33] B. Mortazavi, I.S. Novikov, E.V. Podryabinkin, S. Roche, T. Rabczuk, A.V. Shapeev, X. Zhuang, Exploring phononic properties of two-dimensional materials using machine learning interatomic potentials, Appl. Mater. Today 20 (2020) 100685.

[34] S. Nosé, A unified formulation of the constant temperature molecular dynamics methods, J. Chem. Phys. 81 (1984) 511.

[35] J.K. Nørskov, T. Bligaard, A. Logadottir, J.R. Kitchin, J.G. Chen, S. Pandelov, U. Stimming, Trends in the exchange current for hydrogen evolution, J. Electrochem. Soc. 152 (2005) J23–J26.

[36] X.Y. Yang, A. Banerjee, R. Ahuja, Probing the active sites of newly predicted stable Janus scandium dichalcogenides for photocatalytic water-splitting, Catal. Sci. Technol. 9 (2019) 4981–4989.

[37] D. Gao, B. Xia, Y. Wang, B. Xiao, P. Xi, D. Xue, J. Ding, Dual-Native vacancy activated basal plane and conductivity of $MoSe_2$ with high-efficiency hydrogen evolution reaction, Small 14 (2018) 1704150.

[38] C. Tsai, F. Abild-Pedersen, J.K. Nørskov, Tuning the MoS_2 edge-site activity for hydrogen evolution via support interactions, Nano Lett. 14 (2014) 1381–1387.

[39] R.R. Chianelli, G. Berhault, P. Raybaud, S. Kasztelan, J. Hafner, H. Toulhoat, Periodic trends in hydrodesulfurization: in support of the Sabatier principle, Appl. Catal. A 227 (2002) 83–96.

[40] H.H. Wu, H. Huang, J. Zhong, S. Yu, Q. Zhang, X.C. Zeng, Monolayer triphosphates MP_3 (M=Sn, Ge) with excellent basal catalytic activity for hydrogen evolution reaction, Nanoscale 11 (2019) 12210–12219.

[41] X.F. Zhao, X.Y. Yang, D. Singh, P.K. Panda, W. Luo, Y.X. Li, R. Ahuja, Strain-engineered metal-free $h-B_2O$ monolayer as a mechanocatalyst for photocatalysis and improved hydrogen evolution reaction, J. Phys. Chem. C 124 (2020) 7884–7892.

[42] G.R. Berdiyorov, B. Mortazavi, H. Hamoudia, Anisotropic charge transport in 1D and 2D BeN_4 and MgN_4 nanomaterials: A first-principles study, FlatChem 31 (2022) 100327.

[43] V.B. Zala, R.S. Shukla, A. Bafekry, S.K. Gupta, P.N. Gajjar, In silico study of adsorption of oxide gases by MN_4 (M=Be, Mg) monolayers, Appl. sur. Sci. 605 (2022) 154711.

[44] K.S. Novoselov, A.K. Geim, S.V. Morozov, D. Jiang, M.I. Katsnelson, I.V. Grigorieva, S.V. Dubonos, A.A. Firsov, Two-dimensional gas of massless Dirac fermions in graphene, Nature 438 (2005) 197–200.

[45] Y. Zhang, Y.W. Tan, H.L. Stormer, P. Kim, Experimental observation of the quantum Hall effect and Berry's phase in graphene, Nature 438 (2005) 201204.

[46] X.Y. Yang, J. Wärnå, J. Wang, P. Zhang, W. Luo, R. Ahuja, Enhanced overall water splitting under visible light of MoSSe|WSSe heterojunction by lateral interfacial engineering, J. Catal. 404 (2021) 18–31.

[47] E. Skúlason, V. Tripkovic, M.E. Björketun, S. Gudmundsdóttir, G. Karlberg, J. Rossmeisl, T. Bligaard, H. Jónsson, J.K. Nørskov, Modeling the electrochemical hydrogen oxidation and evolution reactions on the basis of density functional theory calculations, J. Phys. Chem. C 114 (2010) 18182.

[48] H. Wu, X. Li, R. Zhang, J. Yang, Proposal of a stable B_3S nanosheet as an efficient hydrogen evolution catalyst, J. Mater. Chem. A 7 (2019) 3752–3756.

[49] A. Banerjee, S. Chakraborty, N.K. Jena, R. Ahuja, Scrupulous probing of bifunctional catalytic activity of borophene monolayer: Mapping reaction coordinate with charge transfer, ACS Appl. Energy Mater. 1 (2018) 3571–3576.

[50] C. Liu, Z. Dai, J. Zhang, Y. Jin, D. Li, C. Sun, Two-dimensional boron sheets as metal-free catalysts for hydrogen evolution reaction, J. Phys. Chem. C 122 (2018) 19051–19055.

[51] X. Ma, Y. Lv, J. Xu, Y. Liu, R. Zhang, Y.A. Zhu, Strategy of enhancing the photoactivity of $g-C_3N_4$ via doping of nonmetal elements: A first-principles study, J. Phys. Chem. C 116 (2012) 23485–23493.

[52] S. Sinthika, U.V. Waghmare, R. Thapa, Structural and electronic descriptors of catalytic activity of graphene-based materials: First-principles theoretical analysis, Small 14 (2018) 1703609.

[53] G. Gao, Q. Sun, A. Du, Activating catalytic inert basal plane of molybdenum disulfide to optimize hydrogen evolution activity via defect doping and strain engineering, J. Phys. Chem. C 120 (2016) 16761–16766.

[54] Y.R. An, X.L. Fan, Z.F. Luo, W.M. Lau, Nanopolygons of monolayer MS_2: best morphology and size for HER catalysis, Nano Lett. 17 (2017) 368–376.

[55] S. Yu, Y.C. Rao, H.H. Wu, X.M. Duan, C_2N: An excellent catalyst for the hydrogen evolution reaction, Phys. Chem. Chem. Phys. 20 (2018) 27970.